GSA Data Repository Item 2018299

Montalvo, P.E., Cavosie, A.J., Kirkland, C.L., Evans, N.J., McDonald, B.J., Talavera, C., Erickson, T.M., and Lugo-Centeno, C., 2018, Detrital shocked zircon provides first radiometric age constraint (<1472 Ma) for the Santa Fe impact structure, New Mexico, USA: GSA Bulletin, https://doi.org/10.1130/B31761.1.

Data Repository

Item DR1: Additional information on sample locations.

Item DR2: Additional EBSD methods and data.

Item DR3: Additional LA-ICPMS methods and images.

Table DR1: EBSD analytical conditions.

Table DR2: LA-ICPMS U-Pb data.

Item DR1. Additional information on sample locations.

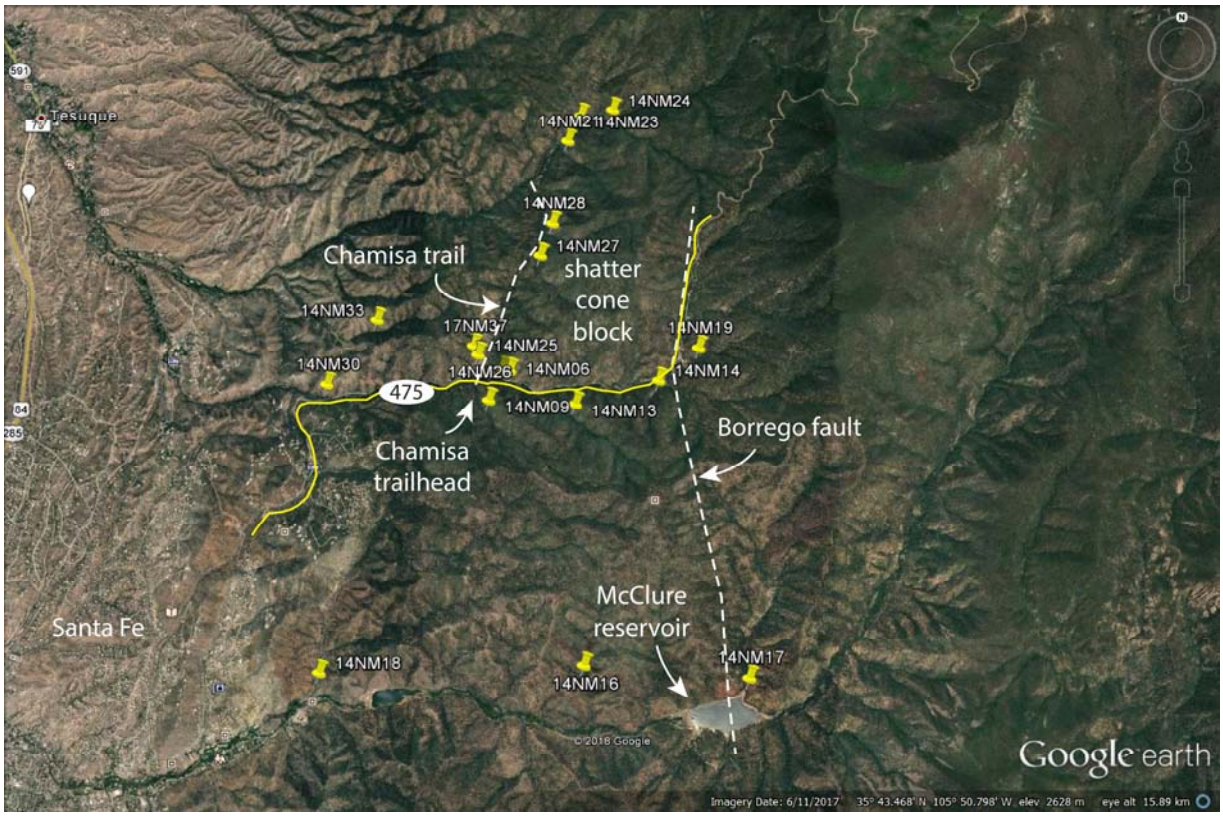

Google Earth satellite image of field area showing location of all 17 samples described in this study. Samples south and east of Highway 475 include 06, 09, 13-14, and 16-19. Samples north and west of Highway 475 include 21, 23-28, 30, 33, and 17NM37. Sediment samples 26 and 30 were collected at sites where breccia is exposed. Samples 14NM06, 14NM25, and 17NM37 are rock samples.

Item DR2. Additional EBSD methods and data.

EBSD analysis was conducted using a Tescan MIRA3 field emission gun (FEG) SEM at the Microscopy and Microanalysis Facility at Curtin University. Automated EBSD maps of regions of interest were generated by indexing electron backscatter diffraction patterns on user-defined grids, and were collected for five zircon grains shown in the main text, and one granular zircon shown below. Maps were collected using step sizes from 50 to 500 nm. EBSD analyses were collected with a 20 kV accelerating voltage, 70° sample tilt, 20.5 mm working distance, and 18 nA beam intensity. Electron backscatter patterns were collected with a Nordlys Nano high-resolution detector and Oxford Instruments Aztec system using routine data acquisition and noise reduction settings (Table DR1; Reddy et al., 2007; see additional examples in Cavosie et al., 2015a,b; 2016a,b). EBSD maps and pole figures were processed using the Tango and Mambo modules in the Oxford Instruments/HKL Channel 5 software package version 5.12. Full EBSD analysis conditions are listed in Table DR1. Each EBSD map included match units for zircon (zircon5260, Mincryst databse card 5260, 1 atm; Hazen and Finger, 1979), quartz (Quartz-new; Sands, 1969) reidite (Reidite6032, 0.69 GPa; Farnan et al., 2003).

Two different EBSD orientation maps are shown in the text. Texture component maps (TC) show angular lattice misorientation relative to a reference point (Figs. 6B,7B; 9D; 10D). All TC maps are overlain on a map showing band contrast, a qualitative measure of the diffraction pattern quality. Dark areas generally indicate low quality diffraction patterns. Inverse pole figure (IPF) maps (Figs. 6-10) show orientation variations that are color-coded to crystallographic axes. Pole figures for significant planes in zircon were plotted as lower hemisphere equal area plots with the same x-y-z reference frame as the EBSD maps.

Boundaries between adjacent pixels that define a {112} twin relationship (65°/<110>) were plotted using the Special Boundary function in Tango. The Special Boundary function allows the user to define a misorientation axis and misorientation angle. For {112} twins in zircon, the misorientation axis is <110>, and the angle is 65°±5°. All {112} boundaries detected are then assigned a colored line (red) (see Figures 6-10).

Table DR1. EBSD analysis conditions.

Sample-grain (14NMxx-xx)	09-31	09-31	09-662	13-336	13-336	26-2	26-2	06-1	06-1	06-1	06-1	16-185
Whole grain (WG) or ROI	WG	ROI	ROI	WG	ROI	WG	ROI	WG	ROI	ROI	ROI	WG
Shown in figure	6B	6C	7D	8D	8E	9D	9E	11B	11C	11D	11E	12B
Duration (minutes)	247	33	122	38	369	694	116	33	9	4.5	6	101
Average mean angular deviation	0.69	0.62	0.57	0.50	0.49	0.51	0.54	0.62	0.75	0.65	0.66	0.66
X steps (pixels)	334	195	219	250	510	592	157	82	60	41	51	264
Y steps (pixels)	471	102	337	126	570	465	222	106	29	38	24	147
Step distance (nm)	200	50	50	500	100	250	50	350	100	100	100	1000
Noise reduction - 'wild spike'	Yes	No	Yes	Yes	Yes	Yes	No	No	No	No	No	Yes
zero solution extrapolation	No	No	No	No	No	No	No	No	No	No	No	No
Kuwahara Filter	No	No	No	No	No	No	No	No	No	No	No	No
SEM Model: Tescan Mira3 FEG-SEM settings												
EBSD system: Nordlys Nano high resolution detector; Oxford Aztec System												
Binning = 4x4; Grain = high; Hough resolution = 60; Band detection (min/max) = 6/8; Background (frames) = 40.												
Carbon coat <5 nm; Acc. Voltage = 20 kV; working distance = 20.5 mm; tilt = 70°; Acquisition speed = 40 Hz												

ROI = region of interest

Item DR3. Additional LA-ICPMS methods and images.

The U-Pb analyses performed via LA-ICPMS were on populations of grains from three samples that contained shocked grains and two others collected nearby those locations. A total of 605 analyses were made on 187 grains from samples 14NM09, 14NM13, 14NM26, 14NM30, and 14NM33. Analytical procedures for U-Pb analysis by LA-ICPMS at the John de Laeter Centre at Curtin have been described elsewhere (e.g., Markwitz et al., 2016) and are briefly summarized here (Item DR3). Spots on individual zircon grains were ablated for 30 s using a 33 µm beam. Dwell time for most elements was 0.01 s, including 0.03 s for Pb isotopes and 0.0125 s for both ^{232}Th and ^{238}U. Glass standard NIST610 was used as the primary standard to calculate elemental concentrations using ^{29}Si as the internal standard element and to correct for instrument drift. Standard analyses were run after every 20 unknown analyses. During time-resolved processing, contamination resulting from inclusions and compositional zoning was monitored, and only the relevant part of the signal was integrated. Trace element results for NIST 612 indicate that accuracy was better than 3% for most elements. Analytical precision was better than 10% for most elements. The primary reference used to calibrate U-Pb data was zircon standard 91500 (1062.4±0.4 Ma; Wiedenbeck et al., 1995); secondary zircon standards include GJ-1 (601.7±1.4 Ma; Jackson et al., 2004) and Plešovice (337.13±0.37 Ma; Sláma et al., 2008). Calculated ^{206}Pb/^{238}U ages for zircon standards were within 3% of accepted values. Time-resolved mass spectra were reduced using the software U-Pb Geochron4 DRS Iolite3.4$_{TM}$ (Paton et al., 2011) and in-house Microsoft Excel macros. All ages are reported with ±2s uncertainties calculated from measured isotopic ratios. ^{204}Pb counts were monitored during the ablation and calculated F204% for accepted analyses were all much less than 0.1%.

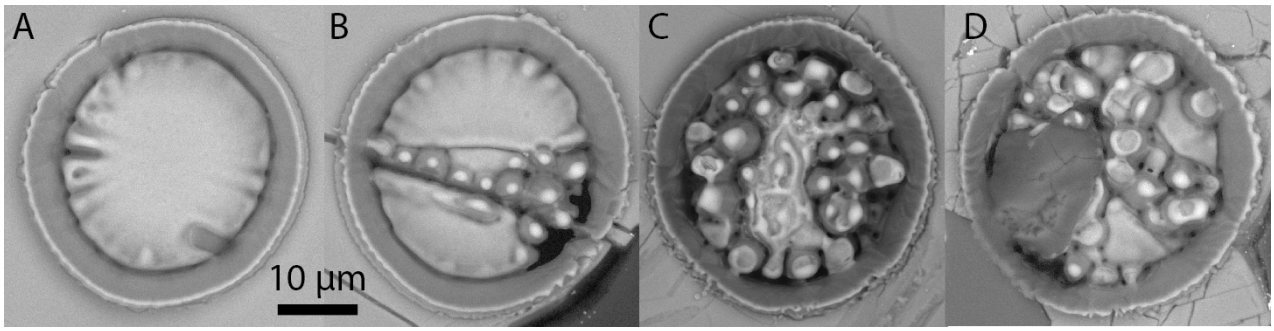

The above BSE images show characteristics of different LA-ICPMS pits made in Santa Fe zircon grains. A: Normal pit. B: Pit with a localized dissocation reaction to SiO_2 + ZrO_2, focused along a crack. C: Pit with pervasive dissociation. D: Pit exposing a quartz inclusion (left side), along with localized dissociation. Pits with characteristics similar to A and B were generally accepted; pits with characteristics similar to C and D were generally rejected.

REFERENCES CITED IN THE DATA REPOSITORY

Cavosie, A.J., Erickson, T.M., and Timms, N.E., 2015a, Nanoscale records of ancient shock deformation: Reidite ($ZrSiO_4$) in sandstone at the Ordovician Rock Elm impact crater: Geology, v. 43, p. 315–318, doi:10.1130/G36489.1.

Cavosie, A.J., Erickson, T.M., Timms, N.E., Reddy, S.M., Talavera, C., Montalvo, S.D., Pincus, M.R., Gibbon, R.J., Moser, D., 2015b, A terrestrial perspective on using *ex situ* shocked zircons to date lunar impacts: Geology, v. 43, p. 999-1002, doi:10.1130/G37059.1.

Cavosie, A.J., Timms, N.E., Erickson, T.M., Hagerty, J.J., and Hörz, F.P., 2016, Transformations to granular zircon revealed: Twinning, reidite, and ZrO_2 in shocked zircon from Meteor Crater (Arizona, USA). Geology, 44, 703-706.

Farnan, I., Balan, E., Pickard, C.J., and Mauri, F., 2003, The effect of radiation damage on local structure in the crystalline fraction of $ZrSiO_4$: investigating the ^{29}Si NMR response to pressure in zircon and reidite: American Mineralogist, v. 88, p. 1663-1667.

Hazen, R.M., Finger, L.W., 1979. Crystal structure and compressibility of zircon at high pressure. Am. Mineral. 64, 196–201.

Jackson, S.E., Pearson, N.J., Griffin, W.L., and Belousova, E.A., 2004, The application of laser ablation-inductively coupled plasma-mass spectrometry to in situ U-Pb zircon geochronology: Chemical Geology, v. 211, no. 1–2, p. 47–69, doi: 10.1016/j.chemgeo.2004.06.017.

Markwitz, V., Kirkland, C.L., and Evans, N.J., 2017, Early Cambrian metamorphic zircon in the northern Pinjarra Orogen: Implications for the structure of the West Australian Craton margin: Lithosphere, v. 9, p. 3-13.

Paton, C., Hellstrom, J., Paul, B., Woodhead, J., and Hergt, J., 2011, Iolite: Freeware for the visualisation and processing of mass spectrometric data: Journal of Analytical Atomic Spectrometry, v. 26, p. 2508–2518, doi: 10.1039 /c1ja10172b.

Reddy, S.M., Timms, N.E., Pantleon, W., and Trimby, P., 2007, Quantitative characterization of plastic deformation of zircon and geological implications: Contributions to Mineralogy and Petrology, v. 153, p. 625-645.

Sands, D.E., 1969. Introduction to Crystallography. WA Benjamin, New York (165 pp).

Sláma, J., Kosler, J., Condon, D.J., Crowley, J.L., Gerdes, A., Hanchar, J.M., Hosrtwood, S.A., Morris, G.A., Nasdala, L., Norberg, N., Schaltegger, U., Schoene, B., Tubrett, M.N., and Whitehouse, M.J., 2008, Plešovice zircon—A new natural reference material for U-Pb and Hf isotopic microanalysis: Chemical Geology, v. 249, no. 1–2, p. 1–35, doi: 10.1016/j.chemgeo.2007.11 .005.

Wiedenbeck, M., Allé, P., Corfu, F., Griffin, W.L., Meier, M., Oberli, F., Quadt, A.V., Roddick,

J.C., and Spiegel, W., 1995, Three natural zircon standards for U-Th-Pb, Lu-Hf, trace element and REE analyses: Geostandards Newsletter, v. 19, no. 1, p. 1–23, doi: 10.1111/j.1751-908X.1995.tb00147.x.